CDKN1A focus formation in mammalian cell nuclei at sites of particle traversal and association with repair or signaling proteins

G. Taucher-Scholz, G. Becker, S. Brons, B. Jakob, M. Scholz and G. Kraft (GSI, Biophysik)

In order to assess the biological endpoints of late radiation effects like genomic instability and transformation it is crucial to understand the signal transduction mechanisms that connect initial DNA lesions with the overall DNA damage response. At the molecular level, high ionization densities result in an increased complexity of DNA lesions leading to an impaired repair ability and extreme cell cycle delays. To gain insight to repair and signaling induced by high-LET radiation, we started monitoring the cellular response within defined subnuclear regions of human cells by examination of immunofluorescence-stained proteins using confocal scanning microscopy. The first protein we studied was CDKN1A (p21), one of the key signaling proteins, known to be induced in an irradiation (x or γ-ray) dependent manner and involved in the arrest of the cell cycle at the G1/S-phase checkpoint [1]. After particle irradiation, CDKN1A showed a rapid formation of localized foci within minutes which are correlated to the sites of ion traversal (Fig.1 left). This correlation was first established on the basis of the Poissonian distribution considering the particle fluence and the individual nuclear area (Fig.1 right) [2].

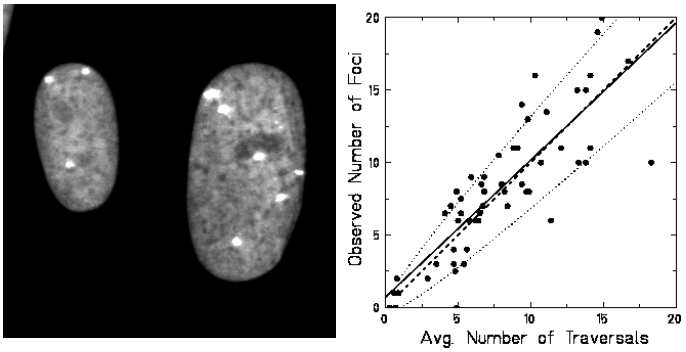

Fig.1 left: Local CDKN1A response (white spots, originally green fluorescence) of human fibroblast nuclei (counterstained with PI, originally red) traversed by uranium ions (9.1 MeV/u) at a fluence of $2.2 \bullet 10^6$ P•cm^{-2}. Size of image: 48 μm. **right:** Correlation between average number of particle traversals of the nucleus and observed number of CDKN1A foci from an experiment with lead ions. Solid line: linear fit to the data; dashed line expected correlation for the ideal case. Dotted lines indicate width of the Poisson distribution around the mean value.

Meanwhile we have obtained direct evidence for the spatial correlation of the nuclear CDKN1A response to particle tracks using broad field particle irradiation in conjunction with the retrospective determination of actual ion traversals through individual cells by track etching [3,4].
The observation that CDKN1A accumulation at sites of damaged DNA persisted for several hours (depending on the LET of the applied particles) before vanishing, indicated a possible function in the processing of radiation induced lesions. The fast translocation of CDKN1A into radiation dependent foci, together with evidence showing that foci are disrupted upon treatment of nuclei with DNAse, point to a new, yet unknown role of CDKN1A in the sensing or processing of DNA lesions generated by high LET particle irradiation. To address this role and to confirm the association to damaged DNA, we studied the response of proteins, known to be involved in different pathways of DNA-repair [5]. The hMre11-protein for example showed a strict correlation of the spatial accumulation to sites of observed CDKN1A foci as detected in differential immunostaining experiments (Fig. 2).

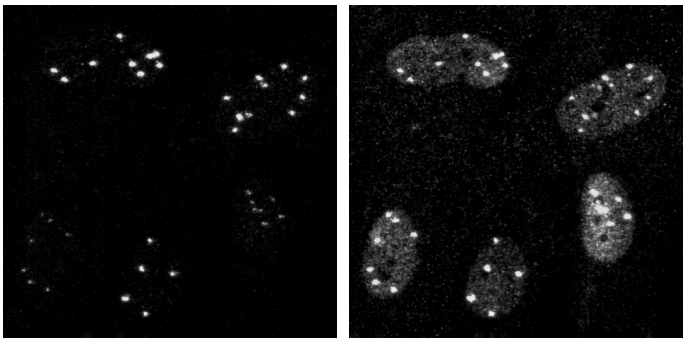

Fig.2 Spatial and temporal colocalization of radiation induced repair foci and CDKN1A in cell nuclei after traversal of gold ions (3.4 MeV/u) at a fluence of $1.9 \bullet 10^6$ P•cm^{-2}. Images were taken from a double immunostained sample and the recording channels were split. **left,** green channel: Immunofluorescence signal of CDKN1A. **right,** red channel: Localization of hMre11 indicating sites of DNA double strand break repair. Notice the identical pattern of bright spots on both images. Size of image: 160 μm.

hMre11 was shown to associate to damaged DNA (especially DSBs) in an heteromeric complex together with Rad50 and the protein mutated in the human autosomal disorder named Nijmegen Breakage Syndrome (NBS1) [6]. Nevertheless, differences in time course of radiation induced protein responses and studies utilizing mutant cell lines lacking functional components of the DNA damage sensing and signaling pathway revealed no direct interaction between examined proteins and CDKN1A foci formed after particle traversal up to now. The proposed new role of CDKN1A in the sensing or processing of radiation induced DNA lesions has therefore to be elucidated in further studies.

References

[1] Elledge S.J., Science 274, 1664-1672 (1996)

[2] Jakob B., Scholz M. and Taucher-Scholz G., Radiat. Res. 154, 398-405 (2000)

[3] Soyland C. and Hassfjell S.P., Radiat. Environ. Biophys. 39, 125-130 (2000)

[4] Scholz et al., Radiat. Res. submitted

[5] manuscript in preparation

[6] Maser R.S. et al. Mol. Cell. Biol. 17, 6087-6096 (1997)

Is the In-Vitro Production of Fibrosis-Associated Signal Protein TGFβ Radiation-Induced?

C. Fournier, P. Sander, G. Taucher-Scholz, G. Kraft (GSI, Darmstadt)

We have investigated whether irradiation of human fibroblasts leads to an enhanced synthesis and secretion of the cytokine TGFβ. Fibrotic in vitro-parameters known to be TGFβ mediated are the accelerated terminal differentiation of fibroblasts and the concomitant enhanced production of proteins [2] both shown to change dose- and LET-dependently [3]. Earlier studies on tissue and animal models reported in literature, revealed a key role of TGFβ in the signal transduction after irradiation resulting in the fibrotic phenotype [reviewed in 1]. Accordingly, the TGFβ-mediated in vitro effects can be suppressed by immuno-neutralisation at non-lethal doses [4,5], but the influence of dose and LET on the expression of TGFβ protein is less pronounced than expected [5,6].

In order to determine the influence of radiation quality on TGFβ synthesis, we irradiated semi-confluent human fibroblasts originating from different tissues (foreskin, skin and lung) with 250 kV x-rays and 11 MeV/u carbon ions (LET 153,5 keV/μm). The total TGFβ content (latent plus activated form) in the cell culture supernatant was measured up to 48 hours after irradiation using an immunoabsorbent assay (ELISA) under serum free conditions or in the presence of 10% fetal calf serum (fcs) containing appr. 8 ng TGFβ per ml. In unirradiated cells the TGFβ amount released into the cell culture medium increases proportionally to cell density, but the calculated production per cell decreases with increasing cell density. This effect is more drastic in the presence of 10% fcs than under serum free conditions (not shown). Under serum-free conditions the cells are arrested in G_1-phase and the cell density remains constant in each flask. After irradiation, the amount of TGFβ per flask increases in controls as well as in irradiated probes independently from dose (not shown). In the presence of 10% fcs the control cells continue to proliferate (1-2 population doublings within 48 hours), whereas the irradiated cells undergo a cell cycle delay, whose duration is dependent on the applied dose, resulting in significantly different cell densities. As shown in figure 1 (top) after 11 MeV/u carbon irradiation, the amount of TGFβ per flask in the presence of 10% fcs increases with time, but independently from dose, leading to an increment of TGFβ per cell (already shown in [5,6]). The observed correlations appear more clearly by directly comparing TGFβ production and cell density (figure 1, bottom): The control cells proliferate and the released TGFβ amount per flask increases proportionally. In contrast, the irradiated cells do not increase in cell density, but attain a comparable level of TGFβ within the same period of time. We could demonstrate this for the three fibroblast cell lines after X-irradiation and for foreskin fibroblasts (AG) after carbon irradiation.

These data confirm our preliminary results after X-irradiation [5] and are in line with data from literature [7]. We could show that the effects are not linked to radiation quality. The data presented sustain our hypothesis, that a fast regulatory step could be the crucial event leading to dose- and LET-dependent changes in fibrosis-related parameters after irradiation [2,5]. The measured changes in TGFβ production after irradiation could be regulated in a subsequent step in a way to assure a constant TGFβ level in the microenvironment of the cells. Such a regulation could normally depend on cell density and become independent from it after irradiation.

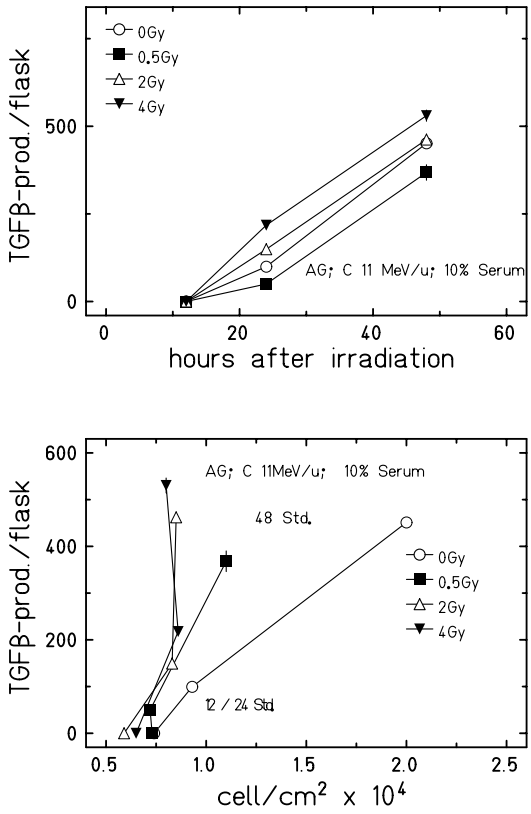

Figure 1: Time-course (top) and influence of cell density (bottom) on TGFβ production in human foreskin fibroblasts after exposure to carbon ions (153,5 keV/μm). Comparable and time-dependent levels of TGFβ are obtained independently of irradiation and concomittant growth inhibition. The increase is measured on top of a basal TGFβ level.

References

[1] Martin, M. *et al.*, Int. J. Radiation Oncology Biol.Phys. 47, 277-290 (2000)

[2] Burger, A. *et al.*, Int. J. Radiat. Biol. 73, 401-408 (1998)

[3] Fournier, C. *et al.*, Int. J. Radiat. Biol. ,in press (2001)

[4] Hakenjos, L. *et al.*, Int. J. Radiat. Biol. 76/4, 503-509 (2000)

[5] Fournier, C. PhD-Thesis (1999)

[6] Fournier, C. *et al.*, GSI-Scientific report 1999, p.156 (2000)

[7] Herskind, C. and Rodemann, H.P., Exp. Gerontol. 35, 747-755 (2000)

Cell and molecular biological analyses of the induction of fibrotic changes in human skin and lung fibroblasts exposed to heavy ion irradiation

H. Peter Rodemann, Oliver Haase,
Section of Radiobiology and Molecular Environmental Research,
Dept. of Radiooncology, Univ. of Tuebingen

As compared to conventional photon radiation heavy ions may offer specific therapeutic advantages in radiation oncology with respect to the higher relative biological effectiveness (RBE) at beam terminus. It has been demonstrated for heavy ion irradiation that the RBE in irradiated normal tissue, especially for acute effects is only slightly increased. However, since normal tissue reactivity, i.e. acute and late effects, is dose limiting in radiation therapy the proposed research project is concerned with the underlying cellular and molecular processes of normal tissue reactivity induced by heavy ions in comparison to photon irradiation. A prominent and clinically highly relevant radiation therapy-induced late reaction of normal tissue is fibrosis [1,2]. Fibrosis can occur especially in skin and lung and is characterized by remodelling of connective tissue resulting in enhanced collagen production and deposition. Although fibrosis is the result of a multicellular process involving endothelial cells smooth muscle cells, immunocompetent cells and fibroblasts within the irradiated tissue, the fibroblast cell system is the cell type responsible for the expression of the fibrotic tissue phenotype. Over the recent years our laboratory could demonstrate that the radiation-induced terminal differentiation of the fibroblast cell system, i.e. the induced differentiation of progenitor fibroblasts to postmitotic highly collagen synthesizing fibrocytes, is the key event in the induction and manifestation of the fibrotic tissue remodelling [3-8]. Molecular biological studies into the basic mechanisms of radiation-induced terminal fibroblast differentiation revealed that the cytokine TGF-β1 is the key factor which mediates the radiation-induced differentiation of progenitor fibroblasts to fibrocytes at the level of signal transduction in an autocrine as well as paracrine fashion. This has been demonstrated in a number of experiments analysing the cellular responses of both normal human or rat skin and lung fibroblasts to ionizing radiation (photons and heavy ions) with and without concomitant treatment with TGFß1-neutralizing antibodies [4-6,9]. Finally, by the use of lung fibroblast cultures from homozygous TGFß1-knock out mice, it could be demonstrated that TGFß1 is the main determinator of fibroblast radiation sensitivity [10].

On the basis of these molecular studies into the cellular mechanism of radiation-induced fibrosis it can be concluded and hypothesized that fibroblasts are stimulated to produce enhanced levels of activated TGFß1 in response to radiation exposure. Activated TGFß1 then binds to the TGFß1 receptor II. In a cascade of phosphorylation reactions several members, i.e. Smad proteins (esp. Smad 4), of the TGFß1-receptor-dependent signal transduction are activated and the TGFß1-signal is transduced to the nucleus. Consequently, the expression of TGFß1-target genes is upregulated resulting in an enhanced expression and activity of the cyclin-dependent kinase inhibitors (cdk-inh.) p21, p27, p15, and p16. Most likely these inhibitors are responsible for the induction of radiation-induced terminal fibroblast differentiation (Rodemann et al. 2001, in prep.). This assumption is based on the observation that TGFß1-neutralizing antibodies can block the long lasting or permanent (>6-8 hrs, TP53 independent) upregulation of p21 expression in response to both radiation and TGFß1-treatment, but not the transient, TP53-dependent p21 expression (< 6 hrs).

The results of the ongoing project will give detailed insights into the regulatory mechanisms of radiation-induced terminal fibroblast differentiation by heavy ions. Together with the results to be established by the Biophysics group at the GSI [11], which investigates the molecular mechanisms and processes of the radiation-dependent activation of the latent inactive form of newly synthesized and secreted LTGFß1, the data will help to describe the specific molecular and cellular pathways, which lead the development of fibrosis in response to radiation exposure. Consequently, these data will not only allow a specific estimation of the risk of fibrosis in radiation therapy applying heavy ions, but also lead to the development of new strategies to prevent or interfere with late normal tissue complications, like fibrosis in radiation oncology.

REFERENCES

[1] Martin M., Lefaix J-L., Pinton P., Crechet F., Daburon F.: Temporal modulation of TGF-ß1 and ß-actin gene expression in pig skin and muscular fibrosis after ionizing radiation. Radiat.Res., 134, 63-70, 1993.

[2] Martin, M., Lefaix, J.-L, Delanian S.: TGF-β1 and radiation fibrosis: a master switch and a specific therapeutic target? Int. J. Radiat. Oncol. Biol. Phys., 47, 277-290, 2000.

[3] Rodemann H.P., Bamberg M.: Cellular basis of radiation-induced fibrosis. Radiother.Oncol., 35, 83-90, 1995a.

[4] Rodemann H.P., Binder A., Burger A., Güven N., Löffler H., Bamberg M.: The underlying cellular mechanism of fibrosis, 1996, Kidney Int., 49, 32-36, 1996.

[5] Burger A., Löffler H., Bamberg M., Rodemann H.P.: Molecular and cellular basis of radiation fibrosis. Int. J. Radiat. Biol. 73:401-408, 1998

[6] Hakenjos L, Bamberg M., Rodemann H.P.: TGFß1-mediated alterations of rat lung fibroblast differentiation resulting in the radiation-induced fibrotic phenotype. Int. J. Radiat. Biol. 76:503-509, 2000a.

[7] Herskind C., Johansen J., Bentzen S. M.,Overgaard M., Overgaard, J., Bamberg M., Rodemann H.P.: Fibroblast differentiation in subcutaneous fibrosis after postmastectomy radiotherapy. Acta Oncologica, 39:383-388, 2000.

[8] Herskind C. and Rodemann H. P.: Spontaneous and radiation-induced differentiation of fibroblasts. Exp. Gerontol. 35:747-755 (2000).

[9] Haase O., Herskind C., Bamberg M., Rodemann H.P.: Can fibroblast cultures be used as a predictive system for radiation-induced fibrosis? Proceedings of Radiation Research 1999, Vol. 2:599-601, 2000a.

[10] von Pfeil A., Hakenjos L., Rodemann H.P.: Radiation sensitivity of mouse lung fibroblasts in vitro is determined by TGF-β1. Int. J. Radiat. Biol., 2001, submitted.

[11] Fournier C., Scholz M., Kraft-Weyrather W., Kraft G., Rodemann H. P.: Changes of fibrosis-related parameters after high and low LET irradiation of fibroblasts. Int. J. Radiat. Biol., 20001, submitted.

Short And Long Term Effects In Human Cells As A Consequence Of High LET Irradiation

J.Kool, B. Klein, M. van Eck-Smaling, A.J. van der Eb and C.Terleth.
Department of Radiation Genetics and Chemical Mutagenesis, Leiden University Medical Centre, Leiden, The Netherlands.

Introduction

In effort to mimick immortalization of human cells, a specific stage of the carcinogenic process *in vitro*, many experimental approaches have been used. Reproducible immortalization could be achieved by transforming human cells with DNA tumor viruses, such as for example SV40 and HPV. The oncogenes largeT and E6/E7 respectively, will modify the human fibroblast's regulatory systems in such a way that the cells will first bypass senescence. Subsequently, during the extended lifespan, the cells will accumulate chromosomal aberrations. Finally, genomic instability will be so massive that the transformed cells enter crisis, a stage defined by massive cell death. Occasionally, at a frequency of 10^{-7}, cells escape crisis and immortalize [1]. Alternatively, immortalization could be achieved by repeated treatments with DNA damaging agents such as 4-NQO and ^{60}Co rays. In these cases, cells would be treated 60-140 times at three day intervals [2]. Our initial interest in irradiating human cells with heavy ions originated from an observation by Dr. Laure Sabatier (CEA,F) that cells which had been exposed to a single high LET irradiation seemed to display an extended lifespan [3]. We wondered whether high LET would indeed lead to such an extension. The molecular basis for the processes discussed above is probably the length of the telomeres. Telomeres are specialized DNA structures at the end of the chromosomes which have a protective role. During the lifespan of the cell telomeres shorten until they reach a certain minimal size, which will trigger senescence. If the cells are forced past senescence, for example by viral oncogenes from DNA tumor viruses, the telomeres will shorten further. At this stage the telomeres become reactive leading to chromosomal instability. For a cell to escape the ensuing crisis, it is necessary to reactivate telomerase, a protein able to stabilize the ends of chromosomes. Indeed, in immortal tumor cells and in *in vitro* immortalized cells telomerase activity is commonly found (although alternative mechanisms of telomere lengthening (ALT) have also been described).

Long term effects

As extension of lifespan is an important step in tumorigenesis, we wanted to determine the effect of high LET irradiation on the lifespan of human cells. Thus we have irradiated normal fibroblasts as well as fibroblasts lacking key factors in installment of senescence (i.e. p16 and p53). In separate experiments, we have irradiated the cells with Ni or Ar, and with different fluences. Subsequently, the cell cultures were closely followed. Population doublings were calculated carefully, samples for RNA, DNA or protein isolations were taken at regular intervals, and chromosome analysis was performed. Results sofar show a gradual, and expected, decrease of telomeres in the cells as population doublings increase. No telomerase is activated and cells enter senescence eventually. In the irradiated cell cultures profound changes can be observed in the chromosomes as a consequence of irradiation, including a delayed genomic instability as has been described previously. The effect of high LET irradiation on lifespan is in this set of experiments very moderate, if significant, with an extension of 3 population doublings at most. However, in one experiment we included a fibroblast line derived from a patient with Nijmegen breakage syndrome (NBS). Interestingly, in these cells a single high LET irradiation has led to an extension of 10 population doublings, which is in the order of magnitude of the effects of the viral oncogenes E6 and E7 from HPV. Even more intriguing, the telomeres in the irradiated cells have increased in the absence of telomerase activity, suggesting activation of ALT. We have recently repeated this experiment including NBS cells from different patients, to see if this a reproducible phenomenon.

Short term effects

When human cells are exposed to irradiation many responses are induced. These responses include the induction of genes, which will eventually lead to processes such as cell cycle arrest, DNA repair or apoptosis. We have focussed in particular on the stress induced pathways involving the MAPkinases. Two kinases play an important role in these pathways; JNK which can activate transcription factors like c-Jun and ATF2, and p38 which can activate ATF-2 [4,5]. We examined activation of the kinases p38 and JNK after irradiation of human cells. Also activation of ATF2 and cJun was examined. In initial studies we have compared the effects of UV and X-rays. Whereas UV is a potent activator of both p38 and JNK, X-rays only weakly activate p38 but not JNK. We then decided to extend our studies to high LET as the RBE might be higher. Initial experiments were performed at GANIL (Caen, F) with Ar, and showed activation of p38 and ATF-2, but no JNK activation. However, our results at GSI for both Ar and C (UniLac and SIS) have been quite different. With Ar we did see clear activation of ATF2 and also cJun, but not of JNK and p38. With C irradiation with a high LET value (135keV/μm) minor activation of ATF2 and cJun was detected but no activation whatsoever could be observed in cells irradiated with C with a lower LET value (27.9keV/μm). Our hypothesis is that the differences seen in activation of the stress responses between irradiated cells are caused by the differences in LET values. It is known that cell survival after irradiation varies with different LET values. Our results suggest that the differences we find after irradiation with different LET values in short term responses, i.e. activation of stress-response pathways, could play a role in the differences seen on survival in the long term.

References

[1] Sedivy JM. (1998). *Proc. Natl. Acad. Sci.*, **95**, 9078-9081

[2] Tsuji T, Miyazaki M, Sakaguchi M, Inoue Y, Namba M. (2000) *Biochem. Biophys. Res. Commun.*, **268**, 20-24

[3] Martins MB, Sabatier L, Ricoul M, Pinton A, Dutrillaux B. (1993) *Mutat. Res.*, **285**, 229-23

[4] Tibbles LA, Woodgett JR. (1999) *Cell. Mol. Life. Sci.*, **55**, 1230-54

[5] Davis RJ. (2000) *Cell*, **103**, 239-252

Low dose hypersensitivity after high-LET irradiation

G. Böhrnsen[1,2], K.J. Weber[2], M. Scholz[1,2]
[1]GSI Darmstadt, [2]Radiologische Klinik Heidelberg

An unexpected hypersensitivity has been reported for several cell lines at low doses (<1Gy), which is not consistent with the linear-quadratic approach currently used in general for the description of survival curves [1,2,3,4]. The corresponding substructure of the survival curves has been attributed to induced radioresistance. There are indications, that high-LET irradiation with neutron or pion beams does not lead to low dose hypersensitivity [1,3], at least in single dose exposure experiments. But no systematic studies on the LET-dependence have yet been performed.

Measurements of low dose effects require high precision assays for the correspondingly high survival levels, where statistical errors represent a principal limit for the accuracy of the standard dilution assay. This problem can be bypassed by using absolute cell counting by means of either cell sorter assays [5] or automated video microscopy assays like e.g. the DMIPS assay [6].

With respect to application of high LET beams in tumor therapy, it is of particular interest, whether hypersensitivity is also observed in situations, which correspond to the radiation quality and dose levels occuring during therapy in the normal tissue in front of the target volume or in the region beyond the tumor. Both regions are characterized by low dose levels due to the inverted depth dose profile or due to beam fragmentation, which contributes to a small dose deposition beyond the tumor. If hypersensitivity is observed in these situations, this could have impact on the RBE values of the normal tissue surrounding the tumor.

In order to investigate the survival after low doses of high-LET radiation, an automated video microscopy system similar to the DMIPS system has thus been developed recently and used for first experiments. The system is able to automatically find the cells without staining using a phase contrast microscope. Cells can then by relocated by means of a computerized microscope stage at regular intervals to follow the fate and growth characteristics of individual cells. Inspection of a flask with approx. 100 cell positions lasts about 20 min; there will be, however, further improvements to accelerate the automatic cell finding and inspection procedures. The measurements include an automatic determination of the colony area, which is - within certain limits - a measure of the cell number per colony. This information can be used to determine growth curves for the individual cells.

The system has been used for experiments at the UNILAC and SIS. First, the agreement of survival curves obtained with the new technique with those obtained using the standard dilution assay has been investigated. No systematic deviations from the results using conventional techniques have been detected for doses higher than 1 Gy for the different radiation qualities.

The system was thus used to investigate in particular the effects of low doses after irradiation with 100 MeV/u carbon ions; the results are summarized in Fig. 1. Up to now, 8 independent experiments have been performed. A significant hypersensitivity at low doses (0.1 Gy) has been detected, whereas for higher doses (0.5 Gy) a transition to the linear-quadratic shape is observed. The general structure of the survival curves closely resembles those reported for low LET irradiation [3] and can be fitted well using a modified LQ-approach including a term for induced resistance [7]. This result is apparently in contrast to the results reported in the literature, where the effect of induced resistance has been reported to be largely reduced e.g. for peak pion irradiation at similar LET values.

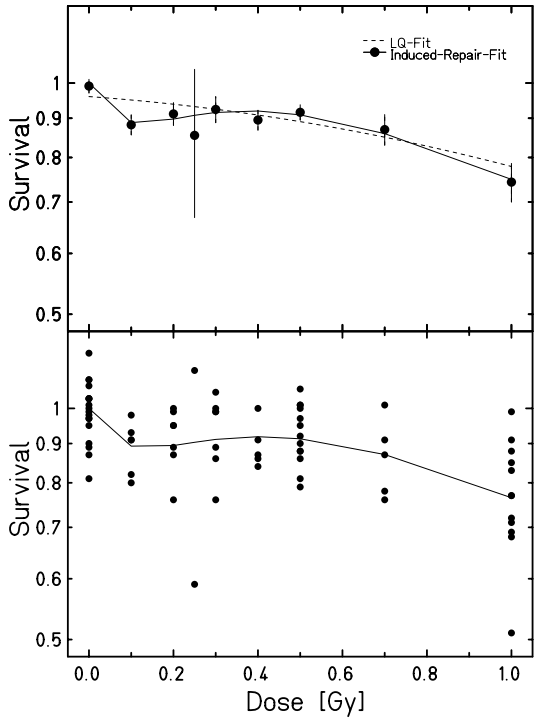

Figure 1: Survival of V79 cells after irradiation with low doses of 100 MeV/u carbon ions. Top: Average values from up to 8 independent experiments. Bottom: Distribution of survival for individual samples. Fits are performed according to an induced repair approach (full line) [7]. For comparison, the backextrapolation from a linear-quadratic fit to the high dose region is shown int the top panel.

References

[1] Lambin P. et al. (1993), Int. J. Radiat. Biol. 63, 639-650
[2] Marples B., Joiner M.C. (1993), Rad. Res. 133, 41-51
[3] Marples B. et al. (1994), Radiat. Res. 138, S81-S84
[4] Singh B. et al. (1994), Int. J. Radiat. Biol. 65, 457-464
[5] Freyer J.P. et al. (1984), Rad. Res. 97, 608-614
[6] Palcic B., Jaggi B. (1986), Int. J. Radiat. Biol. 50, 345-352
[7] Marples, B. Joiner, M.C. (1995), Rad. Res. 141, 160-169

Heavy Ion Irradiation of Human Colon Adenocarcinoma Cells in Multilayer Culture

S. Winhart, W. Müller-Klieser, University of Mainz

M. Scholz, G. Kraft, GSI Darmstadt

Introduction - The major goal of this project is to study the effect of heavy ion irradiation on radioresistant human tumour cells which are grown in a specific tissue-like culture model.

Materials and Methods - WiDr colon adenocarcinoma cells were cultured in either conventional monolayers or cellular multilayers in a specific culture chamber [1]. Cell cultures were irradiated with 250 kV X-rays, with a 100 MeV/u, 200 MeV/u or 400 MeV/u ^{12}C-beam (plateau region), or with an extended Bragg-peak. During irradiation the plane of the mono- and multilayers was positioned perpendicular to the direction of the radiation beam. After radiation, single cell suspensions were derived from the cultures by trypsinisation and appropriate dilution, and these suspensions were used for standardised clonogenic assays. The plating efficiency was determined as the percentage of colonies (>50 cells) in relation to the number of seeded cells, and relative cell survival was determined as a function of radiation dose. Cell cycle analysis was performed with standardised propidium iodide and BrdU labelling techniques and flowcytometry. Apoptoses were detected with a standardised TUNEL labelling using a commercial test kit.

Results - The fraction of apoptotic cells was very low, i. e., around 1 % in untreated cultures and could not be induced by heavy ion irradiation. There was a dose-dependent G_2/M-arrest which was more significant with heavy ions than with x-rays, and which resulted in a G_2-block in 91 % of the cells treated with 6 Gy in the extended Bragg peak. Cell survival rates were lower in monolayer than in multilayer cultures; this phenomenon was most pronounced in the Bragg peak compared to all other radiation conditions, as exemplified in Fig. 1.

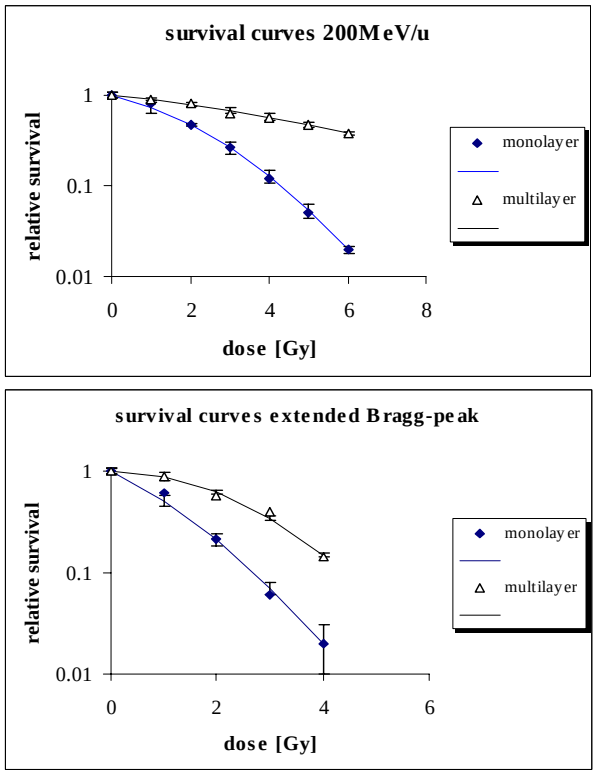

Fig. 1: Relative cell survival as a function of heavy Ion radiation dose in the plateau region (left panel) and in the extended Bragg peak (right panel) for monolayer (diamonds) and multilayer (triangles) cultures.

Discussion – The high radioresistance of WiDr cells compared to most other tumour cell lines can be partially explained by a pronounced G_2/M-arrest following irradiation. This intrinsic resistance is even enhanced by multicellular resistance when cells grow in a in a three-dimensional tissue-like arrangement. The molecular basis of these phenomena need to be investigated.

[1] Minchinton A. I., Wendt K. R. Clow K. A., and Fryer K. H., Acta Oncologica **36**, 13-16 (1997)

Biological effects of 12C - heavy ions on tumor cells

Hana Hofman-Hüther, Margret Rave-Fränk, Patricia Virsik-Köpp

Zentrum Radiologie, Universität Göttingen, Germany

We investigated the induction of chromosome aberrations by carbon ions of different energies in tumor cells of different intrinsic radiosensitivities: MCF-7, an extremely radiosensitive human breast adenocarcinoma cell line and WiDr, an extremely radioresistant colon carcinoma cell line. The aberration yields evaluated in cells in their first post-irradiation metaphase (BrdU-method) were constant independently on the culture time. Carbon ions were in general more efficient with respect to the aberration induction than 200 kV X-rays. The frequencies of dicentric chromosomes and excess acentric fragments were always higher for carbon ions as compared with X-rays in both tumor cell lines. However, in the radioresistant WiDr-cells, a pronounced yield of dicentric chromosomes (about 1 dicentric per cell) could be observed just after irradiation with D = 4 Gy in Bragg peak. Representative aberration data for carbon ions in comparison with X-rays, as observed after irradiation with a dose of 1 Gy are shown in fig. 1

.

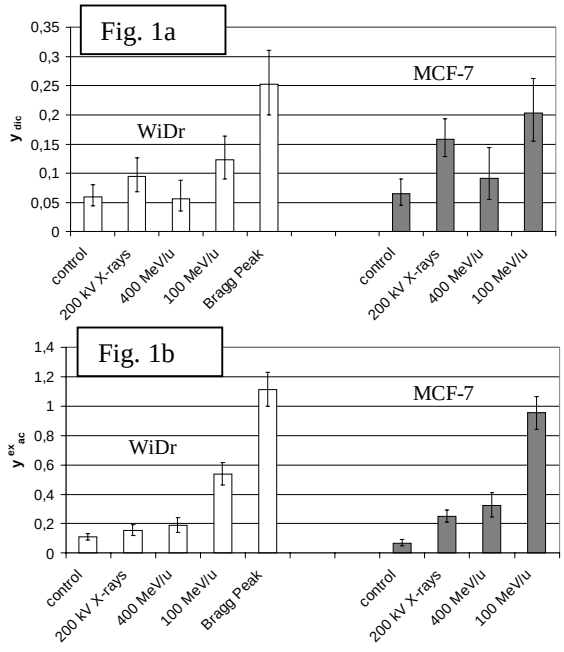

Figure 1: Frequency of dicentric chromosomes (a) and extra acentric fragments (b) per cell scored in first post-irradiation metaphases after irradiation with carbon ions (D=1 Gy) with energies of 400, 100 MeV/u and in Bragg peak, in comparison with 200 kV X-rays.

Using the FISH-method, we scored the radiation-induced simple reciprocal translocations as well as complex exchange aberrations. Since tumor cells are genomically unstable, we first analyzed various chromosomes in both cell lines with respect to their stability. Solely chromosomes No. 2, 4 and 5 were suitable for a FISH-analysis: these chromosomes showed in both unirradiated cell lines either no aberrations or one (or two) stable translocations. The translocation induction was strongly increased for carbon ions as compared with X-rays. Partial translocation yields in WiDr cells irradiated with carbon ions or 200 kV X-rays, as evaluated for chromosome No. 2, are shown as a representative example in fig. 2. Similar results were obtained for chromosomes No. 4 and 5, too. After irradiation with D = 4 Gy, a beginning saturation in the translocation yield could be observed; this is caused by a strong increase in the yield of complex exchanges, as shown in the next figure. Fig. 3 shows the relative proportions of cells containing complex exchanges after irradiation with two different doses of carbon ions or X-rays. Up to 50% of cells irradiated in Bragg peak contained different types of complex exchanges resulting mostly from interactions among 3 different chromosomes.

In summary, a strongly increased biological efficiency of heavy ions is thus confirmed in tumor cells of different intrinsic radiosensitivities with respect to the induction of unstable and stable chromosome aberrations. Moreover, carbon ions induce very efficiently complex exchange aberrations, especially in Bragg peak.

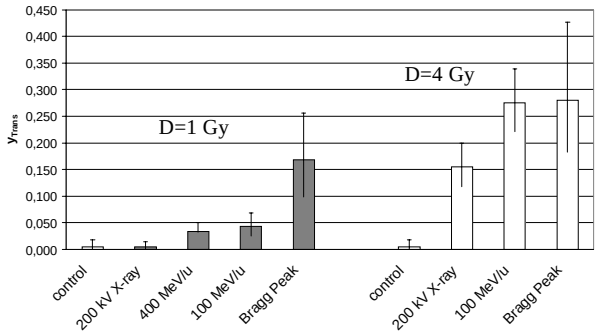

Figure 2: Partial reciprocal translocation yields in WiDr cells, evaluated for chromosome No. 2, irradiated with carbon ions of different energies or 200 kV X -rays.

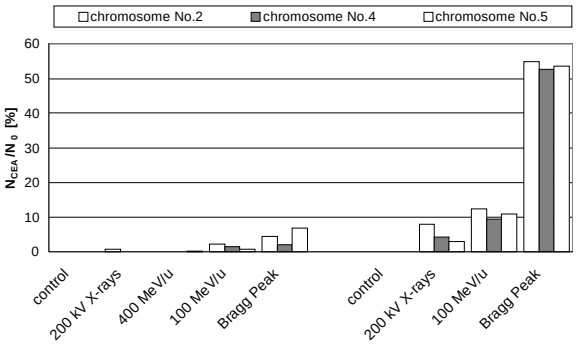

Figure 3: The relative proportions of WiDr cells containing complex exchanges after irradiation with two different doses D=1 Gy and D=4 Gy with carbon ions (100 MeV/u or Bragg peak) in comparison with 200 kV X-rays.

Quantification of High LET Induced Chromosome Aberrations

S. Ritter, S. Berger, T. Größer, P. Hessel G. Kraft (GSI, Darmstadt)
E. Nasonova (JINR, Dubna, Russia), K. Ando (NIRS, Chiba, Japan)
E. Gudowska-Novak (Institute of Physics, Krakow, Poland)

The classical cytogenetic assay relies on the scoring of chromosomal damage in cells at metaphase. According to the standard protocol the analysis is confined to cells at the 1st post-irradiation mitosis collected at one, early sampling time. For sparsely ionizing radiation this protocol allows a reasonable estimate of chromosomal damage, because in all commonly used cell system no or only a slight increase in the aberration yield with time has been observed [1,2 and references therein]. In contrast, as shown in our experiments with different Chinese hamster cell lines [e.g. 1-4] single fixation regimes do not necessarily allow a meaningful quantification of high LET induced cytogenetic damage. Following particle exposure a drastic increase in chromosomal damage with time has been observed. For example, in V79 cells exposed to X-rays the aberration frequency increased by a factor of 3 [1], but in Ar-irradiated samples by a factor of 20 (fig. 1). To account for the time-dependent expression of damage a mathematical approach was used [5], which allows to determine the total amount of aberrations induced within the whole cell population. Based on these total aberration yields RBE values have been calculated. For 10.4 MeV/u Ar (fig. 1) an RBE of 1.9 is obtained. Similarly, for V79 cells exposed to 10.6 MeV/u Ne ions (LET: 390 keV/μm) or 11.1 Kr ions (LET: 3980 keV/μm) RBE values of 3.2 and 1.3 are estimated. As expected, these RBE values are much higher than those reported in the literature [e.g. 6], because in our analysis also drastically delayed heavily damaged cells are included. Moreover, extension of these studies to human primary skin fibroblasts and lymphocytes which are usually used for radiation risk assessment in humans, have shown that the above described effects are not restricted to Chinese hamster cells. For example, in human lymphocytes exposed to 200 MeV/u Fe ions the aberration yield rises in 1st cycle cells by a factor of 7, while after X-irradiation only an increase by a factor of 1.2 is observed.

Furthermore, there is increasing evidence that besides the above described delay of heavily damaged cells additional factors might interfere with the expression of aberrations in metaphase cells. In the case of human lymphocytes apoptosis as well as interdonor variability seem to be important, while in the case of human fibroblasts a permanent cell cycle arrest in G_1 and/or G_2 might contribute to an underestimation of radiation induced damage. For example, as shown in figure 2, even low doses of low LET radiation reduce drastically the number of fibroblasts which are able to proceed to the 1st post-irradiation mitosis. In contrast, this effect is less pronounced for V79 cells which are "apoptosis-resistant" and do not undergo a permanent cell cycle arrest. Even after exposure to 6.5 Gy Kr ions (11.1 MeV/u, 3980 keV/μm) about 50% of V79 cells reach the 1st post-irradiation mitosis and thus can be analysed for chromosomal damage (see fig. 2).

Further experiments are in progress to examine the extent to which interdonor variability as well as high LET induced apoptosis or permanent cell cycle arrest affect the aberration yield detectable in metaphase cells.

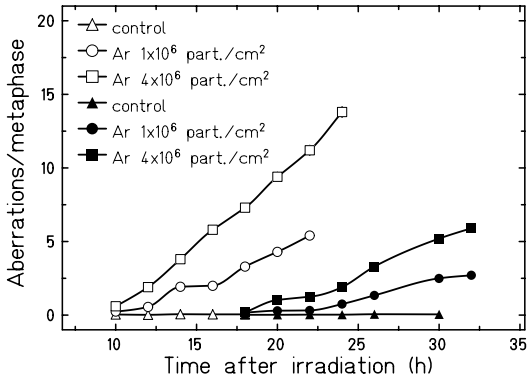

Figure 1: Time-course of aberrations in V79 cells after Ar-irradiation (10.4 MeV/u, 1226 keV/μm). Cells have been exposed in G_1 and chromosomal damage was scored at several sampling times (open symbols: 1st cycle metaphases; closed symbols: 2nd cycle cells). For further details see [3].

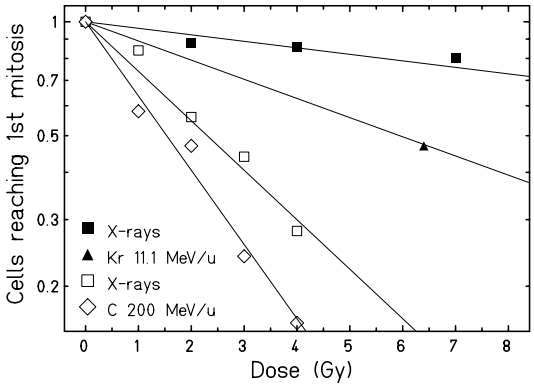

Figure 2: Fractions of human skin fibroblasts (open symbols) and V79 Chinese hamster cells (closed symbols) which reach the 1st post-irradiation mitosis. Human fibroblasts have been exposed to X-rays or 200 MeV/u C ions (LET: 16 keV/μm), V79 cells to X-rays or 11.1 MeV/u Kr ions (LET: 3980 keV/μm). Calculations were performed as described in reference [5].

References

[1] Ritter, S. *et al.*, Int. J. Radiat. Biol. 69, 155-166 (1996)
[2] Nasonova, E. *et al.*, Adv. Space Res. 22, 569-578 (1998)
[3] Ritter, S. *et al.*, Int. J. Radiat. Biol. 76, 149-161 (2000)
[4] Nasonova, E. *et al.*, Phys. Med., in press
[5] Scholz, M. *et al.*, Int. J. Radiat. Biol. 74, 325-331 (1998)
[6] Wu *et al.*, Radiat. Res. 148, S102-S107 (1997)

A comparison of relative biological effectiveness for DNA double strand and mutation induction

J. Kiefer, Strahlenzentrum der Justus-Liebig-Universität, Giessen

We have collected over the years a large date base for heavy ion induced DNA double strand breaks in yeast [1, 2] as well as for the formation of HPRT-mutants in Chinese hamster cells (summarised in [3]). Contrary to findings in mammalian cells [4] DSB induction in yeast cells shows an increase in RBE with LET, displaying a maximum around 100 – 300 keV/µm. Mutation induction is characterised by a qualitatively similar behaviour but with distinctly greater RBE values. In this report both dependencies are compared, results are shown in fig. 1. It is seen that RBE values for both experimental endpoints increase with LET but they are always lower for DSB than for mutation induction.

The broken curves are semi-empirical approximations to the experimental points which are based on the assumption that induction cross sections can be described by a linear-quadratic dependence of the following form

$$\sigma_i = \sigma_0 [1 - \exp - (\alpha L + ßL^2)]$$

with σ_I induction cross section, σ_0 "saturation" cross section, L LET and α, β fitting parameters.

The best fit was obtained with the following values:
Mutation:

$\sigma_i = 11 \times 10^{-7}$ µm^2
$\alpha = 3{,}35 \times 10^{-4}$ µm/keV
ß = 7×10^{-5} (µm/keV)^2

DSB per base pair:

$\sigma_i = 6 \times 10^{-7}$ µm^2
$\alpha = 1{,}54 \times 10^{-3}$ µm/keV
ß = $2{,}85 \times 10^{-5}$ (µm/keV)^2

References

[1] S. Ikpeme, M. Löbrich, T. Akpa, E. Schneider, J. Kiefer, Radiat. Env. Biophys. **34**, 95-99 (1995)
[2] J. Kiefer, R. Egenolf, S. E. Ikpeme, manuscript submitted to Radiat. Res. (2001)
[3] J. Kiefer, Radiat.. Res., in print (2001)
[4] Prise KM, Ahnstrom G, Belli M, Carlsson J, Frankenberg D, Kiefer J, Lobrich M, Michael BD, Nygren J, Simone G, Stenerlow B. Int J Radiat Biol. 74,:173-84 (1998)

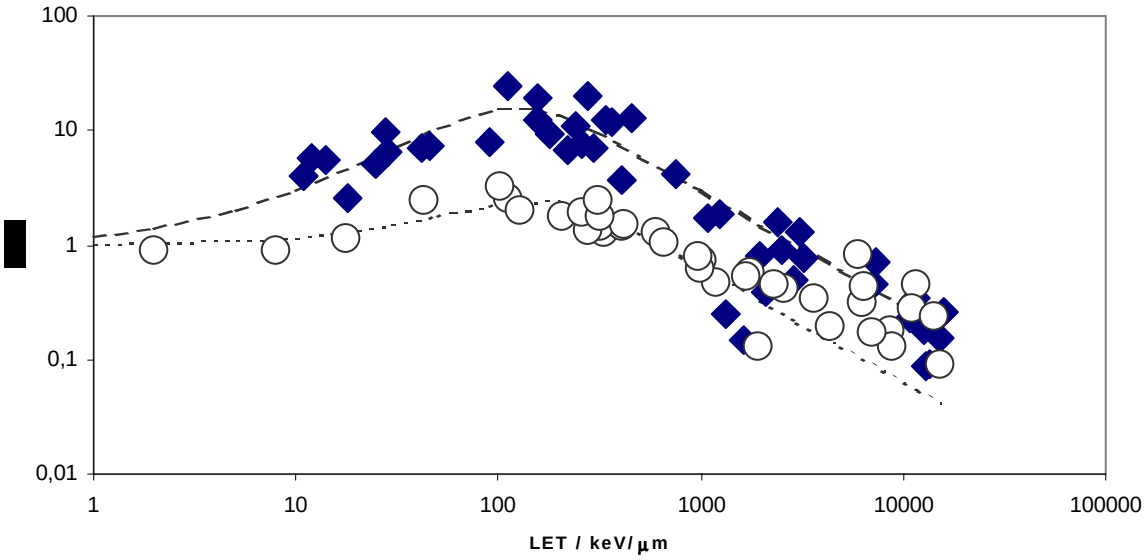

Fig.1: RBE in dependence of LET for DSB (open circles) and mutation induction (rhombi)

Molecular mechanisms of heavy-ion induced radiation damage: Free radicals and products from DNA and chromatin

Barbara Weiland, Anne-Kathrin Hoffmann, Heike Luxenburger and Jürgen Hüttermann, Fachrichtung Biophysik und Phys. Grundlagen der Medizin, Universität des Saarlandes, Klinikum Bau 76, D-66421 Homburg, Germany

Free radical formation in dry DNA and chromatin

A recent EPR analysis of spectra from X-irradiated freeze-dried DNA (77 K to 300°K, 10 kGy to 480 kGy) yielded ten assigned radicals: the oxidized guanine, the reduced thymine and cytosine (two protonation states), the thymine allyl radical, two deoxyribose radicals (C1' and C3'), the 5-thymyl radical, the deprotonated guanine cation and a radical at N7 of a purine [1]. Bombardment with heavy ions (^{50}Ti (11.4 MeV/u), ^{68}Zn (5 MeV/u), ^{197}Au (11.4 MeV/u) and ^{209}Bi (11.4 MeV/u)) at about 100 K confirmed the presence of most primary radicals. The spectra at 9.5 GHz were nearly identical to those after X-irradiation. Dose response curves gave G-values and saturation concentrations in the same order of magnitude [2]. At identical doses, a significant increase of the thymine allyl and the C1' radicals was detected after for heavy ions in aggreement with reports for oxygen impingement [3]. Radical formation in dry chromatin (calf thymus) gave again strong similarities in the EPR spectra after irradiation with either X-rays or heavy ions. Quantitative measurements of pure DNA and of chromatin after X-irradiation together with spectral analysis point at a spin transfer from protein to DNA as was suggested earlier in the literature but was proven only now [4]. The effect of the Bragg-peak was probed specifically by stacking pellets of dry DNA. Xe (11.4 MeV/u) and Ni (6.0 and 11.4 MeV/u) ions were used. For Ni and Xe at 11.4 MeV/u the fourth pellet contains the Bragg-maximum, with Ni at 6.0 MeV/u it is located in the second disk. Fig. 1 shows, that the LET has no effect on the total radical yield in each disk before and in the Bragg-maximum but the amount of thymine allyl radicals as well as C1'- and C3'-deoxyribose radicals increases with LET and dose. The sugar radicals are potential precursors of strand breaks, which in turn are connected with abasic sites.

Product formation in dry DNA

Solid DNA and DNA-nucleotides were used to study the products formed from direct radiation action at 300 K (X-rays and heavy ions in the beam vacuum, respectively). Polycrystalline pyrimidine nucleotides showed the release of unaltered bases as investigated by HPLC and NMR. [5] Further heavy ion experiments with pyrimidine as well as purine nucleotides showed for all these DNA model compounds the formation of the free bases [6]. Recently we found the release of the bases adenine, cytosine and thymine also for dry DNA after heavy ion bombardment. The modified base 8-hydroxy-adenine was identified as another product. X-irradiation and bombardment with Ti (11.4 MeV/u) led to a similar release of unaltered and modified bases, whereas bombardment with Bi (11.4 MeV/u) resulted in a decreasing release of bases. In contrast to the low-LET-irradiation, bombardment with heavy ions effected an increased formation of formate (Fig. 2). This is connected with oxidative sugar dammage and thus is a probe for strandbreaks. The release of bases is also connected with strand breaks in DNA.. If the induced single strand breaks (ssb) appear within few base pairs, a double strand break (dsb) is fromed. The maximum dsb/ssb ratios were calculated for neon and titanium ions. [7] With the assumption that the release of bases and the formation of formate can be connected with a ssb of DNA, we determined a maximum for titanium ions

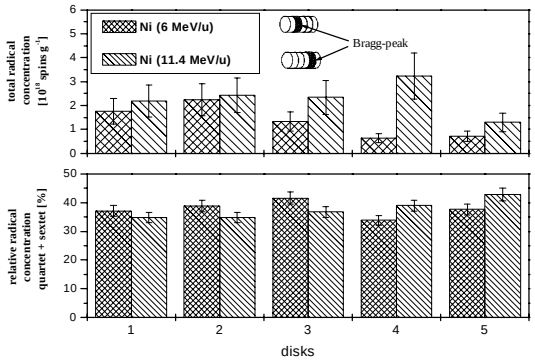

Fig.1 Total and relative radical yield vs. sample thickness

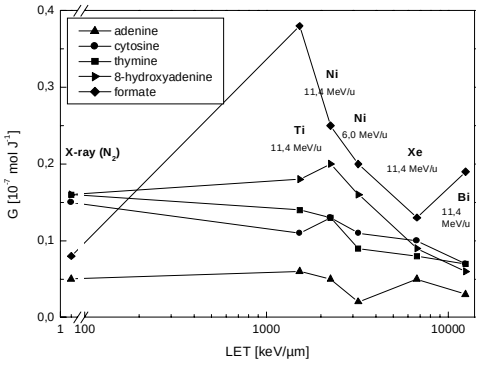

Fig.2 LET-dependence of product formation from DNA

References

[1] B. Weiland and J. Hüttermann, Int. J. Radiat. Biol., 1998, 74, 341-358.

[2] B. Weiland and J. Hüttermann, Int. J. Radiat. Biol., 1999, 1169-1175.

[3] D. Becker et al., Radiat. Res., 1996, 146, 361-368.

[4] B. Weiland and J. Hüttermann, Int. J. Radiat. Biol., 2000, 1075-1084.

[5] A.-K. Hoffmann and J. Hüttermann, Int. J. Radiat. Biol. 1997, 72, 735 - 744.

[6] A.-K. Hoffmann and J. Hüttermann, Int. J. Radiat. Biol. 2000, 76, 1167-1178

[7] [7] J. Heilmann et al., Radiat. Res. 1993, 135, 46-55.

Calculation of depth dose profiles with a track structure code

M. Krämer, GSI

A prerequisite for applying high-LET radiation like protons or carbon ions to patients is the precise knowledge of absorbed dose, specifically the depth dose distribution. The legal restraints imposed by the authorities requires the Bragg peak position to be reproduced within 0.5 mm and the calculated absorbed dose distribution to agree within 5% (on average) with the measurements. These conditions are usually met by our treatment planning code TRiP98 [1, 3] and its builtin beam model [4]. This code uses semi-empirical fragmentation cross sections and external energy loss tables to compute numerically the depth dose distributions. The question now arises whether microscopic Monte Carlo (MC) codes based on single interactions of ions and δ-electrons could reproduce depth dose distributions with similar accuracy. The answer is not obvious since ab-initio simulations would need very accurate primary interaction cross sections.

To address this question an established heavy ion track structure MC code [5] was reworked (TRAX, [6]). In particular, the restriction to track segment conditions has been removed so that ion depth dose profiles can easily be calculated. In addition, other therapy-relevant quantities like ionization yields in dosimetric setups and possibly even W-values could be simulated on a very basic level.

Total and differential elastic scattering cross sections for electrons were fitted to experimental data, as well as the excitation cross sections. Total electron ionization cross sections are calculated according to the relativistic model of Kim [7] with empirical corrections to match low-energy experimental data.

Ion cross sections are contructed semi-empirically as well. The relativistic Kim model was modified for ions to obtain the total ionization cross section, whereas the energy differential δ-electron cross section was evaluated with Rudd's formulae [8]. The angular distribution of δ-electrons was taken from the Binary Encounter Approximation. However, since depth dose distributions are one-dimensional projections and because the path of δ-electrons in water is short compared with the ion penetration depth, the accuracy of the angular distribution plays only a minor role. In contrast to track segment calculations where excitations by ions are usually neglected, these processes have to be included here to obtain reasonable agreement with the established energy loss tables. Since there are no experimental or theoretical data available an empirical approach was chosen by resorting to the electron excitation cross sections with the same velocity.

At first only exploratory calculations were performed, so nuclear fragmentation processes have not been considered, they will certainly be included in future simulations.

A first criterion is the correctness of the energy loss curve compared with the conventional approach. Figure 1 shows the ion energy loss obtained by integrating the δ-electron spectra and adding the binding energy as well as the energy loss from excitation. The agreement with the table used in our planning code is surprisingly good, with local deviations up to 4% in the therapy-relevant energy range from 1 MeV/u to 300 MeV/u. For very high and very low energies deviations are larger.

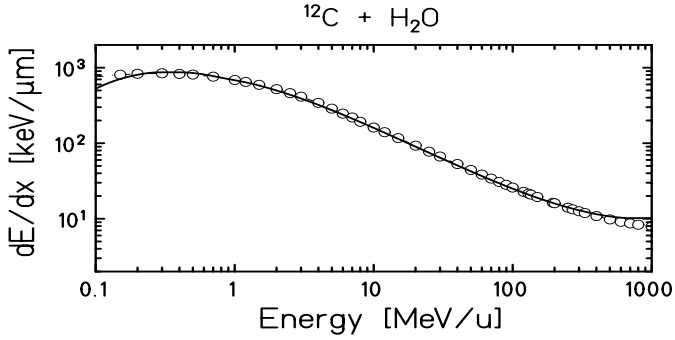

Figure 1: Energy loss for ^{12}C in H_2O. Symbols: from TRiP98, solid line: from TRAX

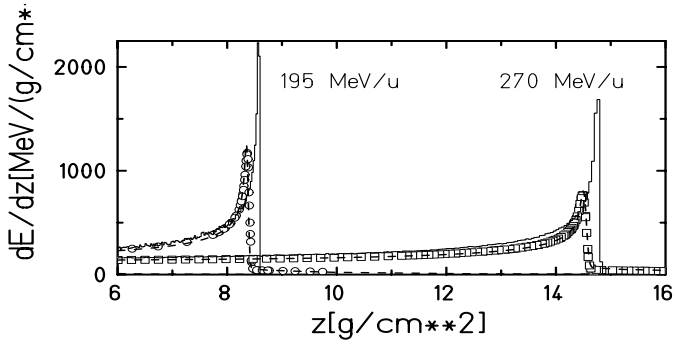

Figure 2: Depth dose profiles of ^{12}C in H_2O. Symbols: experimental data, dashed lines: TRiP98, solid lines: TRAX

Figure 2 compares the present MC results with depth dose calculations from treatment planning as well as experimental data. Bragg peak positions are overestimated by 1.5 to 2.5 mm, this corresponds to a systematic underestimation of the energy loss. Since nuclear fragmentation has not yet been included, the dose values around the Bragg peak are largely overestimated. To bring the MC results in sync with TRiP98 and experiments the ionization and excitation cross sections have to be ameliorated and nuclear fragmentation has to be accounted for.

References

[1] M. Krämer et al, Phys. Med. Biol., 45/11 (2000) 3299
[2] M. Krämer et al, this report
[3] T. Haberer, GSI-report 94-09
[4] M. Krämer, G. Kraft, Rad. Env. Bioph., 33 (1994) 91
[5] http://www.gsi.de/ bio/DOCS/TRAX/DOCS/traxinst.html
[6] Y.-K. Kim, et al., Phys. Rev. A 62 (2000), in press.
[7] M. E. Rudd et al., Rev. Mod. Phys., 64/2 (1992) 441

W-value measurements for carbon ions

J. Rodriguez-Cossio, D. Schardt, C. Brusasco, B. Voss, U. Weber
GSI, Darmstadt

The main error contribution in the absolute dose determination with ionization chambers in the heavy ion therapy comes from the uncertainty on the W-value, which is defined as the average energy required to produce an ion pair in air. For heavy ions, a theoretical approach to the W value is very complex and, moreover, there is a clear lack of experimental data in the energy range of interest in therapy (Fig 1). Even though experimental measurements are difficult if a precision of better than 5% is required, they are still by far the most important and accurate source of W-values.

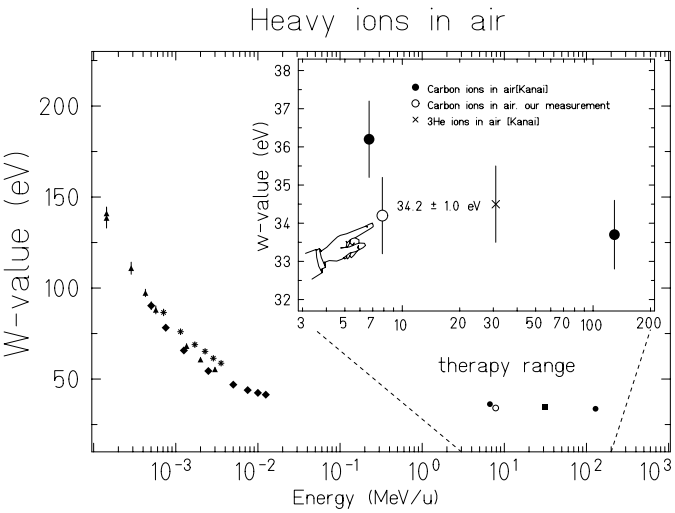

Figure 1: Compilation of the so far available W-value data for heavy ions in air.

In a measurement of the differential W value, three quantities have to be determined independently: the energy E of the incident ions, the mean energy ΔE deposited by one ion when traversing the gas gap and the mean number of ion pairs produced in the gas gap by one ion when dissipating ΔE. This last quantity can be obtained as the ratio of the number of primary ions N_{ions} and the chamber charge output Q, integrated during a certain interval. According to this, the differential W value can be expressed as:

$$w_E = \Delta E \cdot (N_{ions}/Q)$$

The measurements were carried out at the UNILAC target station X6. The beam passed through two double-slit collimators and a thin vacuum window (19 μm Hostaphan) in front of a parallel-plate ionisation chamber (IC) with 14 mm air gap and very thin entrance and exit foils (3,5 μm Mylar each). The energy lost in the vacuum window and in the air gap in front of the IC was calculated using the stopping power code ATIMA. Behind the IC the carbon ions were stopped in a 500 μm thick silicon detector. The energy loss in the air gap of the IC which enters into the w-value was determined as the energy difference observed in the silicon detector spectrum when moving it upstream by the IC gap distance using a precision linear drive.

In a second measurement, the ratio N_{ions}/Q was determined from the charge output of the IC, integrated by an electrometer with high accuracy, and the corresponding number of ions traversing the IC counted simultaneously in a fast scintillator. (Fig.2).

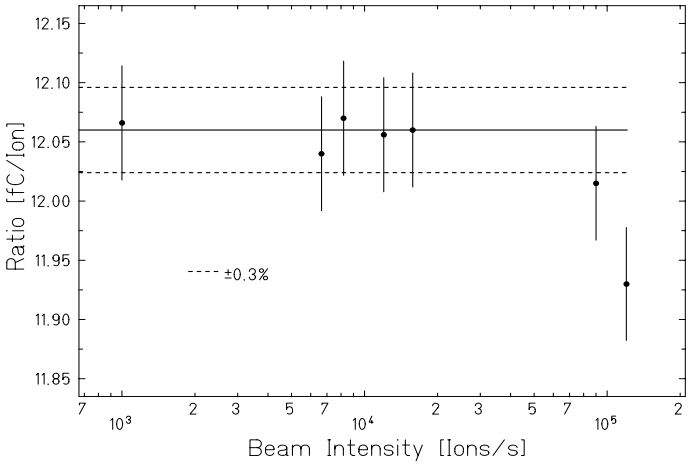

Figure 2: This plot shows the stability of the measured ratio charge per ion counted up to about 10^5 ions/s at the energy of 8 MeV/u. The decrease at higher intensities comes from the increasing relevance of the recombination effect in the chamber.

With this set-up we got the preliminary result :

$$w^{air}_{(7.6\pm0.3)MeV/u\ {}^{12}C^{6+}ions} = (34.2 \pm 1.0)\, eV$$

In comparison with the result of Kanai et al.[1], our value is 6% lower but still in agreement within the given uncertainties as can be seen from Fig.1. The only other data points in the energy range relevant for tumor therapy are those for ^3He at 30 and ^{12}C at 129.4 MeV/u.

For future measurements, an optimised experimental set-up including an ionisation chamber with variable gap length is presently being constructed. The use of a CR39 plastics or diamond detector for the counting of the ions is also being studied for future measurements.

First tests were made at the SIS energy of 200 MeV/u in Cave A. The main findings are the strong build-up effect of the dose (about 5%) and the much weaker initial recombination, as expected, amounting only to a few per mille. The energy loss in the IC for these beam energies is only calculated, becoming a critical point, however, due to the discrepancy between tables when high precision is required.

[1] Kanai et al, Rad. Res. 135 (239), 1993

Fragmentation of High-Energy ^{12}C Ions in Tissue-Equivalent Targets

K.Gunzert, D.Schardt, R.S.Simon and M.Krämer, GSI Darmstadt

A detailed knowledge of the fragmentation properties of primary beam particles penetrating tissue is a major prerequisite for treatment planning in heavy-ion therapy. Projectile fragments are abundantly produced in peripheral nuclear collisions and have in general longer penetration ranges than the primary ions. This leads to a characteristic dose tail beyond the Bragg maximum. Furthermore, the lower-Z fragments have a different relative biological effectiveness as compared to the primary ions. Therefore, the composition of the particle field as a function of depth has to be included into the calculation of the biological effect.

Our earlier fragmentation studies concentrated on the measurement of production rates and angular and momentum distributions of charged particles produced by light ion beams (in particular ^{12}C) penetrating water and other tissue-equivalent targets [1,2,3]. These experiments were continued last year with the investigation of the fast neutron component.

A detector telescope consisting of a 15 cm long, 9 cm in diameter BaF_2 crystal and a 9 mm thin NE102 plastic scintillator in front of it was set up to measure yields, angular distributions and energy spectra of fast neutrons and of charged fragments generated by 100 to 400 MeV ^{12}C ions stopped in thick water, iron and lead targets. The thickness of the targets corresponded to 1.3 times the primary ion range. Operating the NE102 as a veto detector, neutrons can be discriminated from charged particles (mainly protons and α-particles). The neutron energies were measured by time-of-flight (3 m flight path) using a thin start detector (1 mm NE102) in front of the target. The neutron efficiency of the BaF_2 scintillator increases with neutron energy and is nearly constant (about 15%) in the range of 100 to 400 MeV. In collaboration with PTB Braunschweig (V. Dangendorf) the response of the BaF_2 detector was measured in the neutron beams available at Louvain-la-Neuve (Belgium) and Faure (South Africa) with energies of 45 MeV and 100 and 150 MeV respectively.

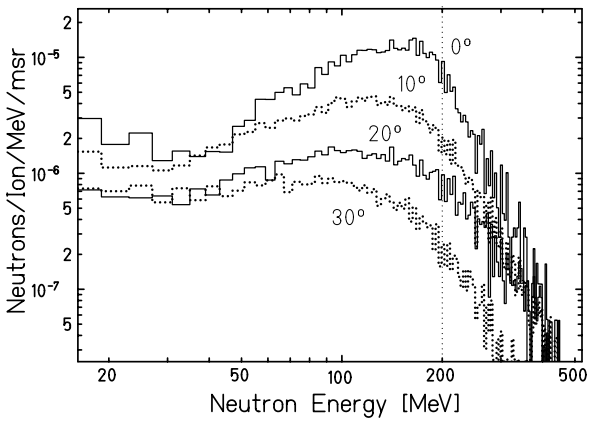

Figure 1: Neutron energy spectra from 200 AMeV ^{12}C ions in a 12.78 g/cm^2 thick water target at different angles.

The neutron energy spectra (Fig.1) show a broad peak at approximately 60% of the initial primary ion energy. This peak becomes more prominent in forward direction and signifies the production of fast neutrons in a break-up process while slower neutrons coming from evaporation processes are isotropically emitted. The fact that neutron energies up to about twice the energy of the incident particle are observed is due to the Fermi energy. These results were found to be in qualitative agreement with similar studies using ^{4}He ions stopped in various thick targets [4]. More recent results with heavier ions were reported in [5,6]. The angular distributions of energy-integrated spectra shown in figure 2 are forward peaked and gaussian shaped. The distributions of the neutrons and hydrogen (inclusive p, d, t) fragments are much broader than that for helium fragments.

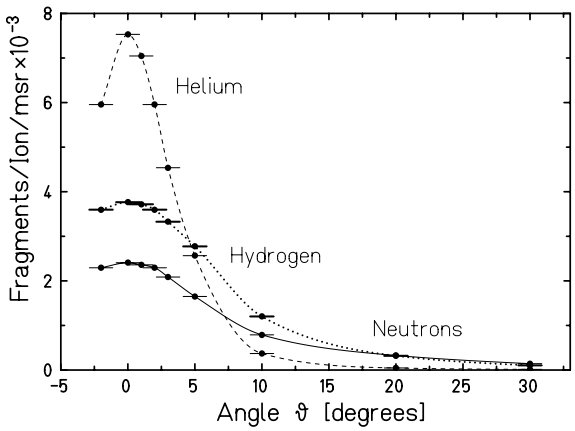

Figure 2: Angular distribution of neutrons, hydrogen and helium fragments produced by a 200 AMeV ^{12}C ion beam in a 12.78 g/cm^2 thick water target.

Besides these studies with phantom targets the characteristic of light particle production in actual patient treatments in Cave M was investigated. The telescope detector was placed 3 m downstream from the patient under polar angles of -5° to +90° degrees. Details of the observed spectra and fragment yields depend on the individual treatment plan, the location of the tumor and the patients anatomy. The aim of these studies is to compare the measured yields of light particles (n, H, He, Li) with those assumed by the physical model which was used for treatment planning.

References

[1] Schardt, D. *et al.*, Adv. Space Res. Vol.17, N^o 2, 87(1996)

[2] Schall, I. *et al.*, NIM B 117,221(1996)

[3] Golovkov, M. *et al.*, Adv. in Hadrontherapy, Elsevier 1997, 316-324

[4] Cecil, R.A. *et al.*, Phys. Rev. C 21, 6, 2471-2484(1980)

[5] Kurosawa, T. *et al.*, Nucl. Sci. Eng. 132, 30-57(1999)

[6] Heilbronn, L. *et al.*, Nucl. Sci. Eng. 132, 2-15(1999)

Corrections of PET Data for Photon Attenuation, Scatter and Positron Range

F. Pönisch, W. Enghardt, B. Naumann; FZ Rossendorf
K. Lauckner; GSI Darmstadt

The evaluation of PET data acquired during ^{12}C therapeutic irradiations initiated a modification of the treatment planning data base improving the precision of the particle range in-vivo [1]. Thus, to an increasing extent delicate therapeutic situations characterized by high dose in close vicinity of organs at risk are treated. The validation of the correctness of such irradiations by means of PET requires precise and reliable methods of data processing. Since the PET control of therapy is based on the comparison of the β^+-activity distributions predicted from the treatment plan with those reconstructed from the data acquired during the patient treatment, both data sets have to be processed the same way. Therefore, the first step of the prediction is a Monte Carlo calculation [2] that describes the stopping of the therapeutic ion beam in tissue, the nuclear fragmentation, the decay of the β^+-emitters, the propagation of positrons and the annihilation photons and finally the γ-ray detection. This code produces a list mode data set like a measurement and thus it can be reconstructed in the same way as measured data.

For the calculation of the positron propagation a new model was developed. Up to now the probability distribution of the positron emitter range was supposed to be a bilinear exponential function [3] with three parameters depending on the maximum positron energy. These parameters have been estimated for β^+-endpoint energies up to 3.5 MeV, which is sufficient for PET applications in nuclear medicine. However, in the nuclear fragmentation reactions between the therapeutic carbon ion beam and the atomic nuclei of the tissue β^+-emitters of much higher endpoint energy (up to 16.7 MeV) are produced for which the parameterization of [3] is not proved. Therefore, the positron range distributions have been calculated by means of GEANT [4] simulations for all positron emitting isotopes that may be produced by the fragmentation of ^{12}C ions in tissue. In Fig. 1 the projection of the 3D spatial distribution on an arbitrary oriented axis (denoted with x) obtained by GEANT is compared with those of Hasch [2] and Derenzo [3]. A look-up table was generated on the basis of the GEANT results. This database is used for the sampling of positron ranges by means of choosing equally distributed random numbers within the interval [0,1].

In the original Monte Carlo code photon scattering was processed in a simplified way by assuming a homogeneous scatter volume (ρ = 1.18 g/cm^3) centred in the field of view (FOV) of the positron camera. Thus, the simulated data had to be reconstructed without attenuation correction. Obviously this approach is quantitatively incorrect and neglects the large tissue inhomogeneities of the head and neck region, as the typical target for carbon ion therapy at GSI. Therefore, a more comprehensive scatter description has been developed. It requires an attenuation map containing the information on the tissue composition and densities within and nearby the camera FOV. These information are derived from the X-ray computed tomograms (CT) of the patient and the head rest CT [5]. The two data sets (Fig. 2) are automatically merged. The created data set is also the basis for the calculation of the attenuation correction factors which are used in the reconstruction. The Fig. 2 shows that there is a significant influence of absorption by the head rest on the detector response leading, if not corrected, to image artefacts in the reconstruction. The dashed lines denote the acceptance cone of the tomograph. Several approaches are applied to the modified code that do not influence the accuracy but reduce the computing time by a factor of 4 in comparison with the original method. The CT based photon scatter estimation allows the reconstruction algorithm to be applied to the measured and simulated PET list mode data in the same way. This is, furthermore, the condition for including a scatter correction algorithm in the reconstruction in order to evaluate both simulated and measured data quantitatively.

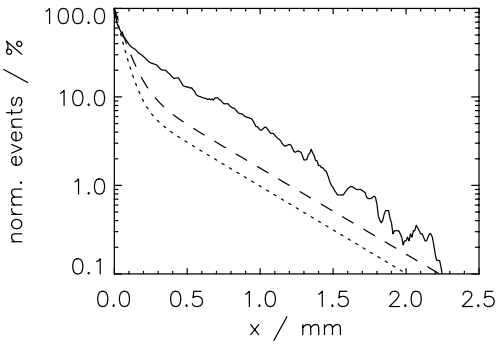

Figure 1: Projections of the positron range distributions for ^{11}C of this work (solid), Derenzo (dashed) and Hasch (dotted)

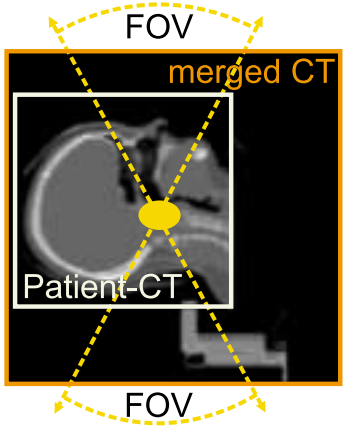

Figure 2: The density distribution for attenuation and scatter correction compared from the patient CT and a CT of the patient support. A possible tumour location and the acceptance cone of the positron camera are displayed.

References

[1] W. Enghardt et al., GSI Scientific Report 1999, 164

[2] B. G. Hasch et al., Annual Report 1996, FZR-179 , 87

[3] S. E. Derenzo, IEEE Trans. Nucl. Sci., 33 (1986), 565

[4] GEANT-Det. Descript., CERN Prog. Lib. W5013, (1994)

[5] F. Pönisch et al., FZR, Annual Report 2000 "An X-ray CT based attenuation correction ...", in press

Positron Emission Tomography (PET) for Ion Therapy Quality Assurance

W. Enghardt, K. Parodi, J. Pawelke, F. Pönisch, M. Sobiella; FZ Rossendorf
P. Crespo, T. Haberer, C. Kausch, K. Lauckner, D. Schardt; GSI Darmstadt

The therapeutic irradiations of 30 patients in 2000 have been observed by PET. The data verified that the modifications of the treatment planning data base [1] considerably improved the precision of dose localization even in delicate situations of very deep-seated and inhomogeneous target volumes (Fig. 1). However, still unpredictable dose deviations may occur because of

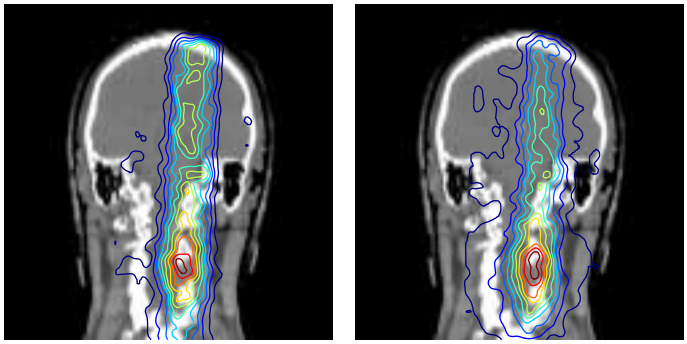

Figure 1: β^+-activity distributions for an irradiation of a tumour in the neck region from cranial, left: prediction from the treatment plan, right: measurement.

minor repositioning errors in connection with sharp density gradients in the beam path or changes in the physical condition of the patient. To quantify such deviations from PET data, improved attenuation, scatter [2] and random [3] correction methods for the measured data as well as refined models (positron range, photon scattering) for predicting the β^+-activity distribution from the treatment plan [2] are introduced. Furthermore, to compensate for the metabolic washout of the positron emitters, which is correlated to the local blood flow [4], the tissue dependent biological half-lives of the β^+-activity have to be known. It is expected that this information can be extracted from the more than 2600 list mode PET data sets measured during patient irradiations so far. An appropriate code that allows the data to be analyzed simultaneously in ordinary space and in the time domain has been developed.

To increase the flexibility in treatment planning the therapy facility will be equipped with a chair [5] for irradiating patients in a sitting position. This required to build a completely new PET gantry (Fig. 2), which allows the detector heads to be rotated around the beam axis [3].

Combining an in-beam PET scanner with an ion beam gantry, as it is planned for the Heidelberg clinical facility, requires new technical solutions, namely new scanner configurations. To predict their imaging properties a versatile PET simulation and reconstruction tool has been developed [3]. Gantry-delivered multi-field irradiations are expected to result in PET scans of low counting statistics, and thus, an optimization of the signal-to-noise ratio is required. For this we studied [6] the possibility of using the new scintillator material lutetium orthosilicate (LSO), which is superior to the currently used bismuth germanate (BGO). This feasibility study was addressed to the influence of background coincidences arising from the β^--decay of ^{176}Lu. Natural Lu contains 2.59 % of this isotope leading to

Figure 2: The new PET gantry. (Photo: A. Zschau, GSI).

an activity of 280 Bq per cm^3 of LSO. However, by means of a correct energy discrimination the influence of the natural activity to the images is eliminated and LSO seems to be a suitable scintillator material for in-beam PET.

In [7] we investigated an extension of the in-beam PET technique to proton therapy monitoring. During accelerator experiments in December 2000 proton beams of 110, 140 and 175 MeV have been delivered to cave M. They have been completely stopped in lucite phantoms positioned in the field of view of the positron camera. Depth distributions of β^+-activity have been measured with good statistics (Fig. 3) and the activity produced by protons has been found to be 3.2 $\pm$ 0.9 as high as that of carbon ions of equal dose and range.

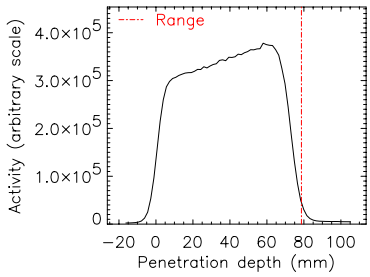

Figure 3: Depth distribution of β^+-activity produced by a proton beam of 110 MeV (range marked by a dashed-dotted line).

References

[1] E. Rietzel et al., Scientific Report 2000, GSI 2000-1, p. 166

[2] F. Pönisch et al., This Report

[3] Annual Report 2000, Institute of Nuclear and Hadron Physics, FZ Rossendorf, Part: Biomedical Research (in press)

[4] R. Hinz, Thesis, Dresden University of Technology, 2000

[5] P. Heeg et al., Scientific Report 2000, GSI 2000-1, p. 167

[6] K. Lauckner et al., IEEE Nucl. Sci. Symp. and Med. Imag. Conf. 2000, Lyon, France, Conference Records

[7] K. Parodi, W. Enghardt, Phys. Med. Biol. 45 (2000) N151

Computer simulations concerning influence of target motion on dose distribution delivered by the GSI raster scanner

Q.Li[1,2] S.Groezinger[1] T.Haberer[1] U.Weber[1] G.Kraft[1]
[1)]GSI Darmstadt, [2)]IMP-CAS Lanzhou

Target motion is a very big problem in conformal radiotherapy (CRT), especiallly for a charged particle beam because of its less lateral scattering and sharp Bragg peak. In the pilot project of the heavy-ion cancer therapy at GSI, patients with head and neck tumors are treated with a magnetic raster scanner[1]. However, if the raster scanner is used to treat patients with body tumors, motion of tumors is present in the lung, breast, liver, kidney and other disease sites, e.g. due to respiration. Therefore, applying the static dose optimization schemes[2] to the moving target by the advanced beam scanning technique could lead to a inhomogeneous dose distribution. So computer simulations about target motion were performed and Gaussian beam profile and sinusoidal movement are assumed as follows,

$$I(x,y) \sim e^{-\frac{x^2+y^2}{2\sigma^2}}, FWHM = \sqrt{8\ln 2}\sigma \quad (1)$$

$$\vec{r}(t) = A_r \sin(2\pi \frac{t}{T_r} + \Phi_0) \cdot \vec{r}_0 \quad (2)$$

here A_r, T_r and Φ_0 are the amplitude, period and initial phase of the movement, respectively. In clinical situation, the average amplitudes of respiration in cranio-caudal and lateral directions are 15mm and 5mm, respectively[3][4]. So maximum displacements of 15mm and 5mm of target volume with 40x40cm^2 in area under beam's eye view along the two different sides were assumed. Realistic raster scanning parameters for the irradiation of the rectangle were supposed, that is, scan stepsizes in x and y directions are 2mm, respectively, and the raster scanner keeps waiting till the prescribed particles have been deposited at a raster point, and then moves to next one with a maximum speed of 10m/s.

The computer simulations were carried out with an experimentally measured beam-spill profile. Fig.1(a) and (b) show the dose distributions for static and moving targets delivered by the raster scanner. It is obvious that the dose homogeneity in the target volume decreases considerably in the case of target motion. In order to assess the inherent variability of dose homogeneity resulting from randomly initial phases, all the calculations repeated 10 times with randomly initial phases and the average values were regarded as the results.

Fig.2(a) shows the relationship between dose homogeneity and rescan at different prescribed particles per raster position. The dose fall-off width through the center of the target volume from the edge to 10% average dose level were also caculated. The dose homogeneity would be improved as the rescan time increases at the expense of the dose fall-off width. Moreover, the increment of dose homogeneity is small and the average dose fall-off widths increase by factors of 2.9 and 1.4 in x and y directions respectively when the rescan exceeds 5 times. In fact, the dose homogeneity will not be better than 82% only by means of rescan for a moving target.

The influence of moving period from 2s to 8s on the dose homogeneity was investigated. The results shows the medial respiratory cycle, for example 4s to 6s, would increase the dose homogeneity when the particle number per raster point is less than 4×10^5. Usually the displacements of target volume due to respiration in different directions are not the same, and the raster scanner has different scanning speeds in horizontal and vertical directions. So the influence of scanning direction along different movement amplitude on dose homogeneity was also evaluated. The result shows if the fast scanning direction (x axis in the simulations) of the raster scanner coincides with that of target movement with large amplitude, for instance the cranio-caudal direction, the dose homogeneity would be improved for prescribed particles per raster point less than 8×10^5 in comparison with the contrary case. When the particle number exceeds this limit, the situation is just contrarious. Different ratios of raster spacing(δ) to FWHM would result in variable dose homogeneity in the static target volume with the raster scanner[1] as shown in the upper part of Fig.2(b). The computer simulations of moving target were made for raster scanning parameter with different δ/FWHM ratios from 0.25 to 0.5. As shown in the lower part of Fig.2(b), it is apparent that the dose homogeneity for raster scanning parameter with large δ/FWHM ratio would be better than that with small one for same specified particles at each raster position

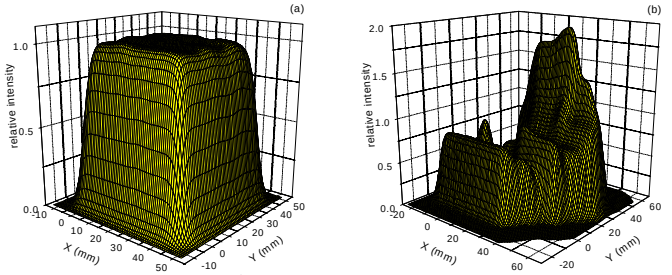

Fig.1 The dose distributions for the static(a) and moving(b) rectangle targets at the particle number per raster position of 5×10^5.

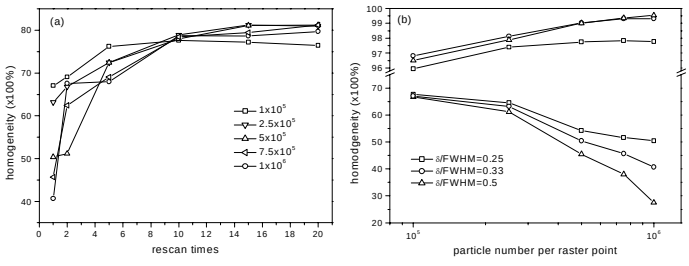

Fig.2 The relationships between dose homogeneity and rescan(a)and ratio of FWHM to raster spacing(b) at differing prescribed particles each raster point.

The simulations here provide a means for evaluating the dose distribution, and the results and implications of this work are being incorporated into the design of a method to compensate for the target motion with the raster scanner at GSI.

References

[1] T.Haberer, et al. Nucl Instrum Meth. A330, 1993:296.

[2] M.Kraemer, et al. Phys Med Biol. 45, 2000:3299.

[3] C.X.Yu, et al. Phys Med Biol. 43, 1998:91.

[4] S.Shimizu, et al. Int J Radiat Oncol Biol Phy. 48, 2000:471.

Treatment planning for the GSI radiotherapy

M. Krämer, C. Brusasco, C. Kausch, E. Rietzel, U. Weber, GSI; O. Jäkel, DKFZ

Throughout the year 2000 our standard treatment planning software TRiP98 [1, 2] which went into production last year [3] was used in combination with the Voxelplan environment for the planning of all 32 patients [4]. Specific improvements on the software side were the introduction of inhomogeneous dose prescriptions, extensions of the beam model and addition of auxiliary functions.

Inhomogeneous dose prescriptions

One major user requirement was the possibility of prescribing partial fields with individually inhomogeneous dose distributions across the target volumes instead of a constant overall weighting of the single fields. The superposition of the partial fields should yield again a homogeneous biologically effective dose distribution. This task was basically solved by allowing to specify 3D dose weighting information. In a first step a weighting cube with a ramp-like dose gradient across the target volume is generated. The gradient should, but need not, be along the beam's eye-view of the irradiation field. Since we have to account for biologically effective dose the initial weighting prescription has to be modified in a second step according to the rules of nonlinear effective dose addition [5] thus yielding two complementary biologically effective 3D weighting distributions. Finally, these distributions are fed into our established single-field optimization procedures, which have been modified to cope with inhomogeneous dose prescriptions instead of a single value. Dose superposition, assessment and verification proceed as usual.

Extensions of the beam model

Our treatment planning code includes a refined and streamlined version of the YIELD beam model [6]. It has been further improved for ^{12}C primary particles by adapting the projectile fragmentation cross sections. It was found that in the vicinity of the Bragg peak heavy fragments were overestimated whereas light fragments were underestimated. This caused a slight overestimation of absorbed and of biologically effective dose beyond the Bragg peak. The improved beam model will be verified and included into the production version in 2001.

Although not verified for primary particles other than ^{12}C our beam model can preliminary be used for treatment planning of lighter projectiles - in view of the upcoming clinic facility. Exploratory calculations showed that there is probably no significant benefit in terms of the ratio of target to entrance (exit) dose for projectiles lighter than carbon, in contrast to other predictions [7].

Miscellaneous improvements

A raster scan path algorithm was introduced which handles irregular patterns of scanner positions - a prerequisite for scanner optimization for moving targets [8].

Another add-on is the evaluation of dose-volume histograms (DVHs) as "figures of merit". Traditionally they are calculated and assessed within the Voxelplan environment. However, with the future multi-field optimization

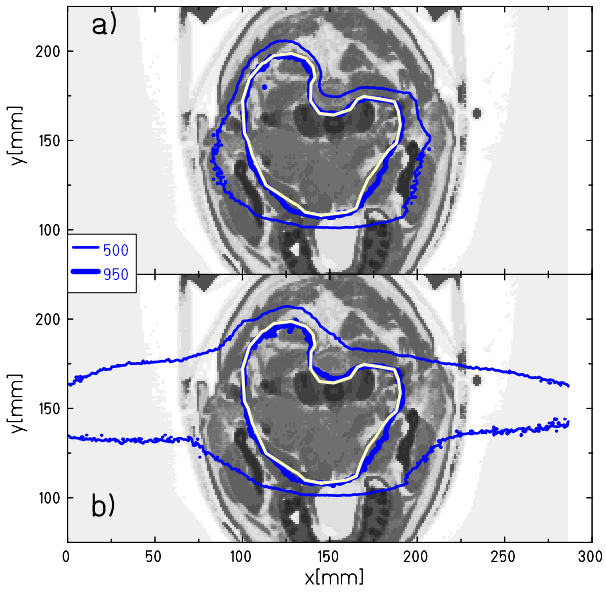

Figure 1: Patient plan with (a) 3 partial dose ramps and with (b) conventional opposing fields. Target as well as 50 and 95% isodoses are shown.

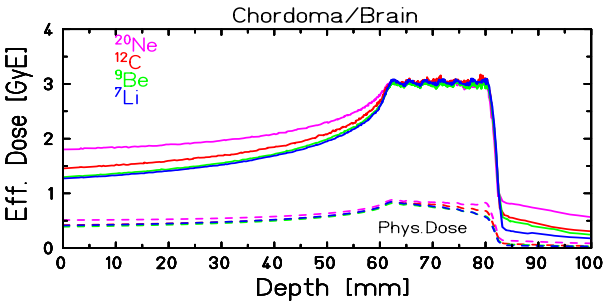

Figure 2: Biological dose profiles for various projectiles

in mind, DVH constraints will be necessary as objective functions for optimization already at the TRiP98 level.

Since the DKFZ CT scanner used since 1997 was replaced by a new one the Hounsfield calibration table had to be revised. Extensive measurements showed that reusing the old table would not lead to significant misalignments.

References

[1] M. Krämer et al, Phys. Med. Biol., 45/11 (2000) 3299
[2] M. Krämer et al, Phys. Med. Biol., 45/11 (2000) 3319
[3] M. Krämer et al, GSI Scientific Report 1999
[4] O. Jäkel et al., Phys. Med. Biol., 46 (2001), in press
[5] M. Krämer, J. Radiat. Res. 41/4 (2000), in press
[6] T. Haberer, GSI-report 94-09
[7] A. Brahme, GSI-report 2000-04
[8] Q. Li et al, this report

Heavy-Ion Therapy at GSI: Progress Report

Th. Haberer, J. Debus, H. Eickhoff, W. Enghardt, P. Heeg, G. Kraft, D. Schardt

GSI Darmstadt, Radiologische Klinik Heidelberg, FZ Rossendorf, DKFZ Heidelberg

Clinical Trials

In 2000 three Carbon beam blocks were used to treat 32 patients suffering from skull base tumors such as chordomas, chondrosarcomas, adenoid cystic carcinomas and other less frequent indications. Partially these ongoing clinical trials have reached phase II level. In total 73 patients have been treated within this experimental programme and the overwhelming part of treatments had a curative intention [1,2]. The very promising local control rate as well as the low treatment related toxicity rate kick off new clinical goals like a dose escalation or the treatment of extracranial locations. In preparation of treatments in the pelvic region a dedicated immobilization device was tested at GSI (see figure 1) and the mandatory approval is under way.

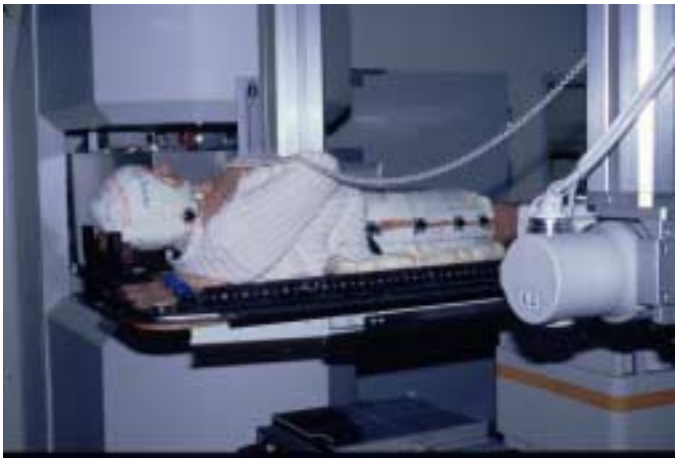

Figure 1: Patient in a rigid immobilization device adapted for the patient couch of GSI's medical cave.

Physical-technical Aspects

In the third year of routine operation ≈ 20% of the SIS-beamtime were used to operate the medical cave for 13 weeks in a time-sharing mode with physics experiments. The performance of the GSI accelerators reached an excellent level of more than 95% beam availability.
The limited angle positron camera BASTEI [3] installed at our treatment facility was upgraded to be rotatable (see figure 2). This feature will allow the use of the PET-method in combination with the patient chair which presently is under commissioning and should be operational by the end of 2001 [4]. This additional functionality will extend the variety of entrance channels thus offering the possibility of treating more patients and further reduce the unavoidable dose to the organs at risk.

Figure 2: The nozzle of the treatment facility with the rotatable head of the PET camera.

References

[1] J. Debus et al., Strahlentherapie und Onkologie, 2000, 176(5): 211–216
[2] D. Schulz-Ertner et al., this report
[3] R. Hinz et al., Physica Medica **XIII/1**,1997, p. 61
[4] P. Heeg at al., GSI annual report 1999

Patient irradiations at GSI

D. Schulz-Ertner, C. Thilmann, M. Wannenmacher, J. Debus

Before patient irradiations started in 1997, a radiation unit was built at the heavy ion synchrotron of the GSI and major future directed technical and radiobiological innovations have been implemented. For the first time, tumor conform application of carbon beams was realized by intensity-controlled rasterscanning with pulse-to-pulse energy variation [1]. All patients had 3D treatment planning including a biological plan optimization using the treatment planning program TRIP developed at GSI [2]. A PET camera is used for online beam verification [3].

Up to now, 73 patients with tumors of the skull base and the brain have been treated with carbon ions. The study mainly contained patients with chordomas (33) and low grade chondrosarcomas (16) of the skull base, adenoid cystic carcinomas (8) and malignant meningiomas (8). These tumors are known to be relatively radioresistant against conventional photon irradiation. Proton radiotherapy has been shown to improve outcome in chordomas and low grade chondrosarcomas [4] but its availability is limited. In adenoid cystic carcinomas radiation therapy with heavy particles as neutrons results in improved local control rates compared to photon irradiation but causes severe side effects [5]. Malignant meningeomas commonly recur within the former irradiated fields even after high tumor doses. Carbon ion therapy presents a promising therapy option in the management of these tumors.

Within the feasibility study, median tumor dose was 60 GyE in chordomas and chondrosarcomas. Patients with adenoid cystic carcinomas and malignant meningiomas received fractionated stereotactic photon irradiation at Heidelberg University with a median dose of 50.4 Gy and a carbon ion boost with 18 GyE (6 x 3.0 GyE) to the gross tumor. Feasibility of this new therapy approach has been shown. First results are very promising with a local control rate of 94% at 1 year [6]. We observed a partial tumor regression in 7 of 33 patients treated for chordoma indicating that carbon ion therapy is effective in these tumors (figure 1+2). Tumor regression in chordomas is a finding which is rarely reported in literature after any kind of radiation therapy. Besides, active beam delivery using raster scanning allows for highly conformal dose distributions and therefore results in an optimal sparing of neighbouring normal tissue. The low toxicity rate allows further dose escalation. As a consequence the total tumor dose has been escalated from 60 GyE to 70 GyE for chordomas and chondrosarcomas in the following phase II study which has been activated in November 2000. A rigid immobilization device developed by Lohr et al.at DKFZ [7] has been tested at GSI and will guarantee the safe irradiation of extracranial tumors. In 2001 a phase I/II study for the treatment of sacral / spinal chordomas and low grade chondrosarcomas will be activated. Furthermore, photon irradiation with a carbon ion boost will be available within a clinical phase I/II study for adenoid cystic carcinomas in 2001.

Figure 1+2. Chordoma of the skull base a) prior to RT, b) 3 months after RT with carbon ions.

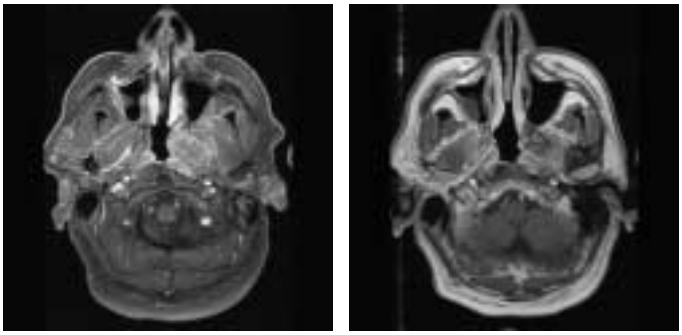

References

[1] Haberer T et al. Magnetic scanning system for heavy ion thrapy. Nucl Inst Phys Res 1993; 330:296-305.

[2] Scholz M et al. Cell cycle delays induced by heavy ion irradiation of synchronous mammilian cells. Int J Radiat Oncol Biol Phys 1994; 66:59-75.

[3] Enghardt W et al. The application of PET to quality assurance of heavy ion tumor therapy. Strahlenther Onkol 1999; 175:Suppl II:33-36.

[4] Munzenrider JE et al. Proton therapy for tumors of the skull base. Strahlenther Onkol 1999; 175:Suppl II:57-63.

[5] Krull A et al. Neutron therapy in malignant salivary gland tumors: results at European centers. Recent Res Cancer Res 1998; 150:88-99.

[6] Debus J et al. Carbon ion irradiation of skull base tumors at GSI. First clinical results and future perspectives. Strahlenther Onkol 2000; 176(5):211-216.

[7] Lohr et al. Noninvasive patient fixation for extracranial stereotactic radiotherapy. Int J Radiat Oncol Biol Phys 1999; 45(2):521-527.